Springer

KSME

Journal of Mechanical Science and Technology 26 (5) (2012) 1355~1361
www.springerlink.com/content/1738-494x
DOI 10.1007/s12206-012-0331-9

Finite element simulation of blood flow in a flexible carotid artery bifurcation †

Sang Hoon Lee[1], Hyoung Gwon Choi[2,*], Jung Yul Yoo1[1]

[1]*School of Mechanical and Aerospace Engineering, Seoul National University, Seoul, Korea*
[2]*Department of Mechanical Engineering, Seoul National University of Science and Technology, Seoul, Korea*

(Manuscript Received October 10, 2011; Revised February 12, 2012; Accepted March 20, 2012)

Abstract

Numerical simulations for the blood flow are carried out to investigate the effect of the flexible artery wall on the flow field and to determine the wall shear stresses in the carotid artery wall. To solve the equation of motion for the structure in typical fluid-structure interaction (FSI) problems, it is necessary to calculate the fluid force on the surface of the structure explicitly. To avoid complexity due to the necessity of additional mechanical constraints, we use the combined formulation including both the fluid and structure equations of motion into a single coupled variational equation. The Navier-Stokes equations for fluid flow are solved using a P2P1 Galerkin finite element method (FEM) and mesh movement is achieved using arbitrary Lagrangian-Eulerian (ALE) formulation. The Newmark method is employed to solve the dynamic equilibrium equations for linear elastic solid mechanics. The time-dependent, three-dimensional, incompressible flows of Newtonian fluids constrained in the flexible wall are analyzed. The study shows strongly skewed axial velocity and flow separation in the internal carotid artery (ICA). Flow separation results in locally low wall shear stress. Further, strong secondary motion in the ICA is observed.

Keywords: Carotid artery; Blood flow; Fluid-structure interaction; Finite element method

1. Introduction

It is well known that atherosclerotic plaque tends to generate and develop in carotid artery sinus. Localized atherosclerotic lesions are associated with low wall shear stress regions [1] and many researches account for the cause of atherosclerosis. Bharadvaj et al. [2, 3] developed a standard geometry using 57 actual geometries and studied the flow characteristics of steady state flow in the carotid bifurcation. Perktold et al. computed the flow in different carotid bifurcation geometries [4] and considered non-Newtonian fluid properties [5]. Also, Pulsatile flow in a 3D flexible carotid bifurcation is simulated using a pressure correction finite element method [6], and the velocity profiles and the wall shear stress distributions are compared with the experimental results from Ku et al. [7].

For better descriptions of the flow in carotid bifurcation, more realistic approaches are required. Recently, multidimensional 3D-1D model of the whole arterial tree has been developed for more realistic boundary waveforms [8]. The model includes a 3D finite element model for carotid bifurcation coupled with a simple 1D model for the rest of the arterial tree, and good agreement between the results of 3D-1D combined model and a pure 1D model was obtained. Kim et al. [9] studied gravitational effect on wall shear stress distribution in carotid bifurcation and cerebral arteries and observed that gravitational effect has a significant influence on the arterial deformation. The flow field in the vessel would be highly influenced by the properties of the vessel wall. Thus, the flexibility of the vessel wall is one important factor for the flow fields in carotid bifurcation.

The fluid-structure interaction problem is usually solved in a partitioned way [10-12]. The FSI problems are solved sequentially in a partitioned way, and the displacement and traction at the fluid-structure interface have to be calculated. On the other hand, a monolithic approach used in the present study is relatively simple so that both fluid and structure equations are formulated using velocity variables [13, 14]. As velocity variables are shared, kinematic constraint is automatically satisfied. In the present study, flow characteristics in carotid bifurcation are analyzed in a monolithic FSI approach.

2. Numerical methods

For monolithic approach of fluid-structure interaction problems, incompressible Navier-Stokes equations are adopted in Lagrangian form for structure. Incompressible Navier-Stokes equations in arbitrary Lagrangian-Eulerian form are as follows:

*Corresponding author. Tel.: +82 2 979 6312, Fax.: +82 2 949 1458
E-mail address: hgchoi@snut.ac.kr
† This paper was presented at the AJK2011, Hamamatsu, Japan, July 2011. Recommended by Guest Editor Hyon Kook Myong and Associate Editor Do Hyoung Lee.

$$\nabla \cdot \mathbf{v}^f = 0,$$
$$\rho^f \left[\frac{\partial \mathbf{v}^f}{\partial t} + \left(\mathbf{v}^f - \mathbf{v}^m \right) \cdot \nabla \mathbf{v}^f \right] = -\nabla p + \nabla \cdot \boldsymbol{\tau} \tag{1}$$

where ρ^f, v^f, v^m, p and τ denote fluid density, fluid velocity, mesh velocity, pressure and shear stress tensor, respectively. Linear elastic equations for the structure are as follows:

$$\rho^s \frac{\partial^2 \mathbf{u}^s}{\partial t^2} = \nabla \cdot \boldsymbol{\sigma} + \mathbf{f} \tag{2}$$

where ρ^s, u^s, σ and f denote density, displacement, stress tensor of structure and volume forces, respectively.

2.1 Spatial discretization

P2/P1 finite elements are used to discretize governing equations, and their weak forms are as follows:

$$\int_{\Omega_f} q \nabla \cdot \mathbf{v}^f d\Omega = 0,$$
$$\int_{\Omega_f} \left[\mathbf{w} \cdot \rho^f \frac{\partial \mathbf{v}^f}{\partial t} + \tilde{\mathbf{w}} \cdot \rho^f \left\{ \left(\mathbf{v}^f - \mathbf{v}^m \right) \cdot \nabla \mathbf{v}^f \right\} \right. \tag{3}$$
$$\left. + \nabla \mathbf{w} : \left(-p\mathbf{I} + \boldsymbol{\tau} \right) \right] d\Omega \quad - \int_{\Gamma} \mathbf{w} \cdot \left\{ \left(-p\mathbf{I} + \boldsymbol{\tau} \right) \cdot \mathbf{n} \right\} d\Gamma = 0,$$

$$\int_{\Omega_s} \mathbf{w} \cdot \rho^s \frac{\partial^2 \mathbf{u}^s}{\partial t^2} d\Omega + \int_{\Omega_s} \nabla \mathbf{w} : \boldsymbol{\sigma} d\Omega$$
$$= \int_{\Gamma} \mathbf{w} \cdot \left(\boldsymbol{\sigma} \cdot \mathbf{n} \right) d\Gamma + \int_{\Omega_s} \mathbf{w} \cdot \mathbf{f} d\Omega \tag{4}$$

where q and w are weight functions for the continuity and momentum equations, which are of first and second order, respectively. Pressure variables are defined only on the vertexes, and velocity variables are defined on all vertexes and midpoints. To stabilize the equations for high Reynolds number flows, streamline upwind/Petrov-Galerkin method [15] is applied to the convection term of fluid equations. The modified weight function for the convection term is as follows:

$$\tilde{\mathbf{w}} = \mathbf{w} + \frac{\alpha h_e}{2 \left| \mathbf{v}^f \right|_e} \left(\mathbf{v}^f - \mathbf{v}^m \right) \cdot \nabla \mathbf{w},$$
$$\alpha = \begin{cases} \gamma / 6 & 0 < \gamma < 3 \\ 1/2 & 3 < \gamma \end{cases}, \quad \gamma = \frac{\rho^f \left| \mathbf{v}^f \right|_e h_e}{2\mu}. \tag{5}$$

γ is cell Peclet number and h_e is the element characteristic length.

2.2 Temporal discretization

To discretize the governing equations in time, Generalized-α method is used [16]. Quantities related to the time derivative of primary unknowns are evaluated at the generalized midpoint α_m, while unknowns themselves are evaluated at the generalized midpoint α_f, as follows:

$$\left(\frac{\partial \mathbf{v}^f}{\partial t} \right)^{n+1-\alpha_m} = \left(1 - \alpha_m \right) \left(\frac{\partial \mathbf{v}^f}{\partial t} \right)^{n+1} + \alpha_m \left(\frac{\partial \mathbf{v}^f}{\partial t} \right)^{n}, \tag{6}$$

$$\left\{ -\rho^f \left(\mathbf{v}^f - \mathbf{v}^m \right) \cdot \nabla \mathbf{v}^f + \nabla \cdot \boldsymbol{\tau} \right\}^{n+1-\alpha_f}$$
$$= \left(1 - \alpha_f \right) \left\{ -\rho^f \left(\mathbf{v}^f - \mathbf{v}^m \right) \cdot \nabla \mathbf{v}^f + \nabla \cdot \boldsymbol{\tau} \right\}^{n+1} \tag{7}$$
$$+ \alpha_f \left\{ -\rho^f \left(\mathbf{v}^f - \mathbf{v}^m \right) \cdot \nabla \mathbf{v}^f + \nabla \cdot \boldsymbol{\tau} \right\}^{n}.$$

Using generalized midpoints in time, Eqs. (3) and (4) can be described in matrix form as follows:

$$\left[\mathbf{G}^f \right]^{\mathrm{T}} \left(\mathbf{v}^f \right)^{n+1-\alpha_f} = 0,$$
$$\left[\mathbf{M}^f \right] \left(\frac{\partial \mathbf{v}^f}{\partial t} \right)^{n+1-\alpha_m} + \left[\mathbf{C}^f + \mathbf{D}^f \right] \left(\mathbf{v}^f \right)^{n+1-\alpha_f} \tag{8}$$
$$+ \left[\mathbf{G}^f \right] \left(p^f \right)^{n+1} = \left[\mathbf{F}^f \right]^{n+1-\alpha_f},$$

$$\left[\mathbf{M}^s \right] \left(\frac{\partial \mathbf{v}^s}{\partial t} \right)^{n+1-\alpha_m} + \left[\mathbf{K}^s \right] \left(\mathbf{u}^s \right)^{n+1-\alpha_f} = \left[\mathbf{F}^s \right]^{n+1-\alpha_f}. \tag{9}$$

Accelerations and displacements in each equation are described as velocity variables by the Newmark approximations as follows:

$$\left(\frac{\partial \mathbf{v}}{\partial t} \right)^{n+1} = \frac{1}{\gamma \Delta t} \left(\mathbf{v}^{n+1} - \mathbf{v}^n \right) - \frac{1-\gamma}{\gamma} \left(\frac{\partial \mathbf{v}}{\partial t} \right)^{n}, \tag{10}$$

$$\mathbf{u}^{n+1} = \mathbf{u}^n + \frac{\Delta t}{\gamma} \left[\beta \mathbf{v}^{n+1} + \left(\gamma - \beta \right) \mathbf{v}^n \right]$$
$$+ \frac{\Delta t^2}{2\gamma} \left(\gamma - 2\beta \right) \left(\frac{\partial \mathbf{v}}{\partial t} \right)^{n}. \tag{11}$$

Finally, the governing Eqs. (1) and (2) are temporally semi-discretized as follows:

$$\left[\mathbf{G}^f \right]^{\mathrm{T}} \left(\mathbf{v}^f \right)^{n+1-\alpha_f} = 0,$$
$$\left\{ \frac{\left(1 - \alpha_m \right)}{\gamma \Delta t} \left[\mathbf{M}^f \right] + \left(1 - \alpha_f \right) \left[\mathbf{C}^f + \mathbf{D}^f \right] \right\} \left(\mathbf{v}^f \right)^{n+1}$$
$$+ \left[\mathbf{G}^f \right] \left(p^f \right)^{n+1} = \left[\mathbf{M}^f \right] \left\{ \frac{\left(1 - \alpha_m \right)}{\gamma \Delta t} \left(\mathbf{v}^f \right)^{n} \right. \tag{12}$$
$$\left. + \left[\frac{\left(1 - \alpha_m \right)\left(1 - \gamma \right)}{\gamma} - \alpha_m \right] \left(\frac{\partial \mathbf{v}^f}{\partial t} \right)^{n} \right\}$$
$$- \alpha_f \left[\mathbf{C}^f + \mathbf{D}^f \right] \left(\mathbf{v}^f \right)^{n} + \left[\mathbf{F}^f \right]^{n+1-\alpha_f},$$

$$\left\{ \frac{1 - \alpha_m}{\gamma \Delta t} \left[\mathbf{M}^s \right] + \frac{\left(1 - \alpha_f \right) \beta \Delta t}{\gamma} \left[\mathbf{K}^s \right] \right\} \left(\mathbf{v}^s \right)^{n+1}$$
$$= \left[\mathbf{F}^s \right]^{n+1-\alpha_f} + \left[\mathbf{M}^s \right] \left\{ \frac{1 - \alpha_m}{\gamma \Delta t} \left(\mathbf{v}^s \right)^{n} \right. \tag{13}$$

$$+\left[\frac{(1-\alpha_m)(1-\gamma)}{\gamma}-\alpha_m\right]\left(\frac{\partial \mathbf{v}^s}{\partial t}\right)^n\Bigg\}$$
$$+\left[\mathbf{K}^s\right]\Bigg[-\left(\mathbf{u}^s\right)^n-\frac{(1-\alpha_f)(\gamma-\beta)\Delta t}{\gamma}\left(\mathbf{v}^s\right)^n$$
$$-\frac{(1-\alpha_f)(\gamma-2\beta)\Delta t^2}{2\gamma}\left(\frac{\partial \mathbf{v}^s}{\partial t}\right)^n\Bigg].$$

The parameters α_f, α_m, β and γ in temporal discretization method are optimized for control of high frequency dissipation in the fluid and structure systems, respectively. The optimal choice of the parameters for the fluid equation which is of first order is as follows [17]:

$$\alpha_m=\frac{1}{2}\frac{3\rho_\infty-1}{1+\rho_\infty},\ \alpha_f=\frac{\rho_\infty}{1+\rho_\infty},\ \gamma=\frac{1}{2}-\alpha_m+\alpha_f. \tag{14}$$

For the structure, the optimal parameters are different as the system is of second order [16].

$$\alpha_m=\frac{2\rho_\infty-1}{1+\rho_\infty},\ \alpha_f=\frac{\rho_\infty}{1+\rho_\infty},\ \gamma=\frac{1}{2}-\alpha_m+\alpha_f,$$
$$\beta=\frac{1}{4}\left[1--\alpha_m+\alpha_f\right]^2 \tag{15}$$

where ρ_∞ is spectral radius for an infinite time step.

2.3 Coupling of fluid and structure equations

One of the difficulties in coupling fluid and structure equations is that information such as displacements and stresses must be exchanged at the interface. To simplify the coupling procedure in this study, both equations are formulated using velocity variables which are shared at fluid-structure interface [13, 14]. As velocity variables are shared, kinematic constraint is automatically satisfied. Stress terms $[F_s]$ and $[F_f]$ between fluid and structure do not have to be calculated explicitly for compatibility of stress terms at the fluid-structure interface, as they are balanced when Eqs. (12) and (13) are summed. The flowchart of the numerical procedure is shown in Fig. 1.

3. Model validation

For model validation, wave propagation in a straight flexible tube [18-20] has been simulated. The properties and basic geometries are selected to be close to that of blood flow in a large artery: D = 0.02 m, wall thickness = 0.002 m, length = 0.1 m, E = 1 x 10^6 Pa, ν = 0.3, $\rho^f = \rho^s$ = 1 x 10^3 kg/m^3, fluid viscosity μ = 4 x 10^{-3} Ns/m^2. The schematic of tube geometry is shown in Fig. 2, where tetrahedral finite elements about 67,000 for the fluid region and about 38,000 for the flexible wall are used in the calculation. The initial conditions of the total system were p = 0 Pa, U = 0 m/s. At t = 0 a step change in pressure is applied at the left end of the tube to the system.

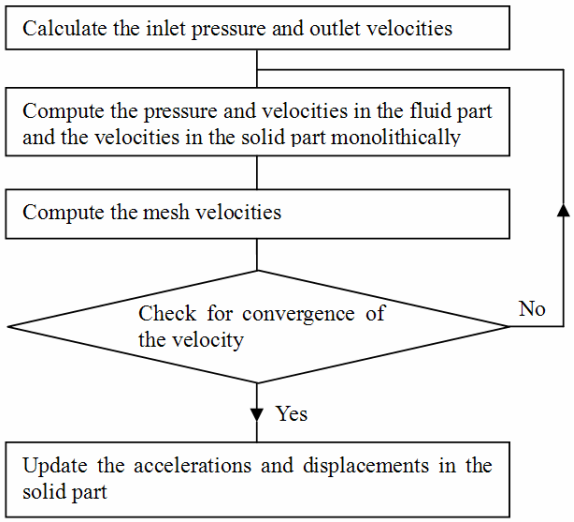

Fig. 1. Flowchart of numerical procedure.

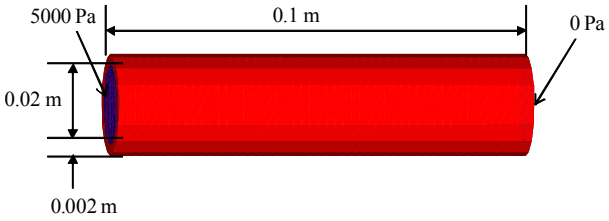

Fig. 2. Schematic of tube geometry.

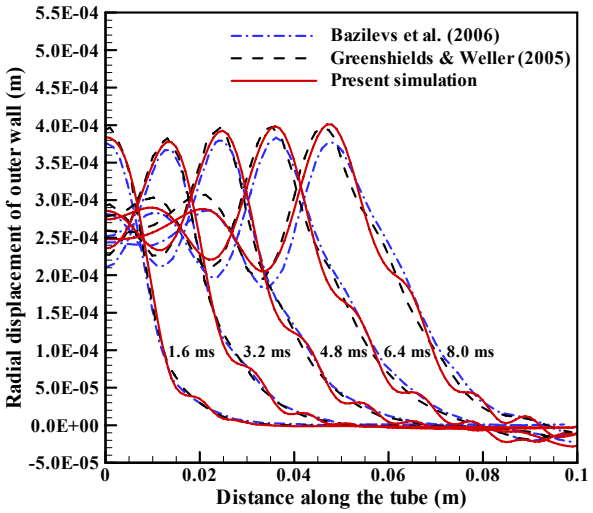

Fig. 3. Radial displacement of outer wall along tube [18, 19].

Then the pressure wave propagates downstream through the tube. The simulation results of outer wall displacement are compared with previous calculations [18, 19] in Fig. 3, where the results are in fairly good agreement. The predicted wave speed is only 1.3% lower than the wave speed of the analytic solution of the present case. The small oscillations downstream of the largest peak are shown in Fig. 3. The wiggles also appeared in the incompressible flow calculation of Jog

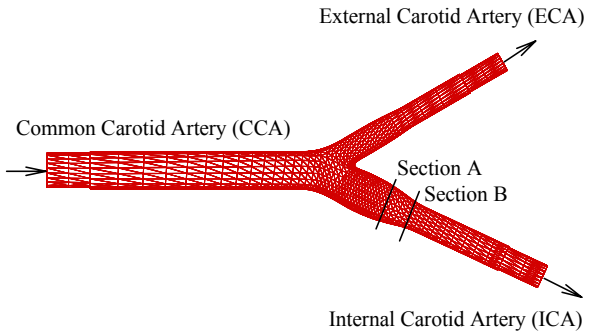

Fig. 4. Schematic of carotid bifurcation.

and Pal [20], where a 40 × 24 quadrilateral mesh and $\Delta t = 10^{-4}$ s were used. As shown in Fig. 3(b) of Kang et al. [21], the radial displacement at t = 8.0 ms is in good qualitative agreement with that of Jog and Pal [20] along the tube length, except that there is some discrepancy upstream of the largest peak, which may be due to the lack of spatial resolution in their calculation. These oscillations are believed to appear due to perturbations that propagate faster than the peak.

4. Results and discussion

4.1 Steady-state flow in a carotid bifurcation

Fig. 4 shows the schematic of the present carotid bifurcation model. Numerical simulations were conducted using the same flow conditions as those in the experiment of Gijsen et al. [22]. The Reynolds number at the inlet of CCA was 270 and flow division ratio defined by the flow rate of ECA over CCA was 0.45. Newtonian fluid was considered with fluid density ρ = 1.41 x 10^3 kg/m^3, fluid viscosity μ = 2.9 x 10^{-3} Ns/m^2. No-slip boundary condition was applied at the wall and parabolic velocity profiles were imposed at the inlet and outlet velocities. Tetrahedral finite elements used in the calculation about 28,000 for the fluid region and about 8,000 for the flexible wall. Axial velocity distribution was measured at section A and B (Fig. 5) which are positioned apart from the apex as two and five times of the radius of CCA , respectively. High shear rates are shown near the divider wall and low shear rates exist near the non-divider wall. The low velocity near the non-divider wall is caused by an adverse pressure gradient due to the increase of the cross-sectional area as shown in Fig. 6. Further downstream, axial velocity profile previously flattened is recovered near the non-divider wall and velocity peak moves to the near the divider wall because the cross-sectional area decreases as shown in Fig. 5. Comparison with previous results show fairly good agreement. The shapes and sizes of axial velocity profiles are quite similar.

4.2 Pulsatile flow in a carotid bifurcation

Pulsatile flow through the same carotid bifurcation model was calculated. The waveforms of pressure and flow rate were

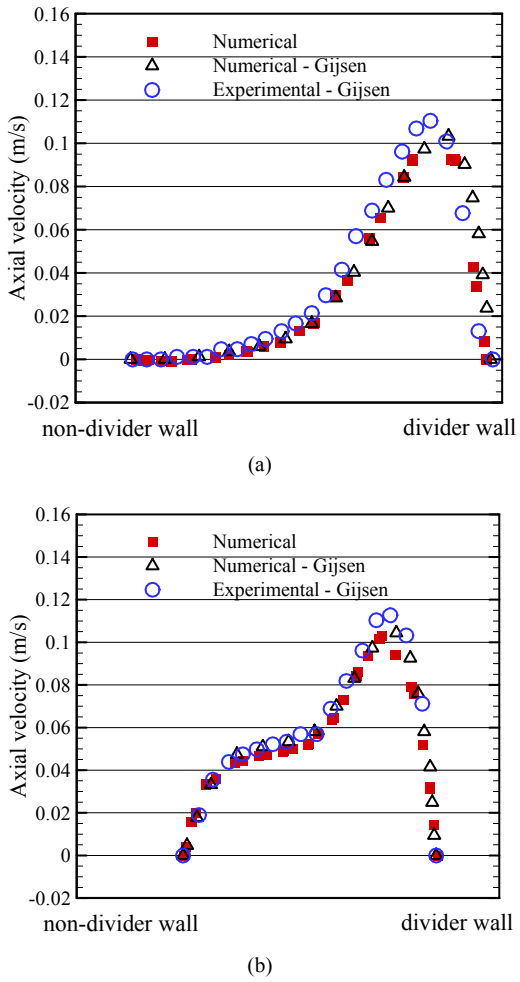

Fig. 5. The axial velocity distribution: (a) Section A; (b) Section B [22].

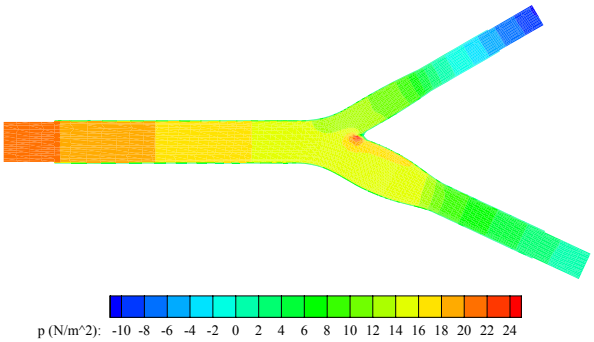

Fig. 6. pressure contour at mid-plane.

assigned the same waveforms of Tada & Tarbell [23] as shown in Fig. 7. Pressure is imposed at the inlet, and the outlet pressure is calculated from the solution of the Navier-Stokes equations. That is, no B.C. for outlet pressure is necessary since all velocity components are given at the exit. The blood in the carotid artery was considered as a Newtonian fluid because non-Newtonian fluids have a small effect on pulsatile blood flow in large arteries such as the carotid artery [24].

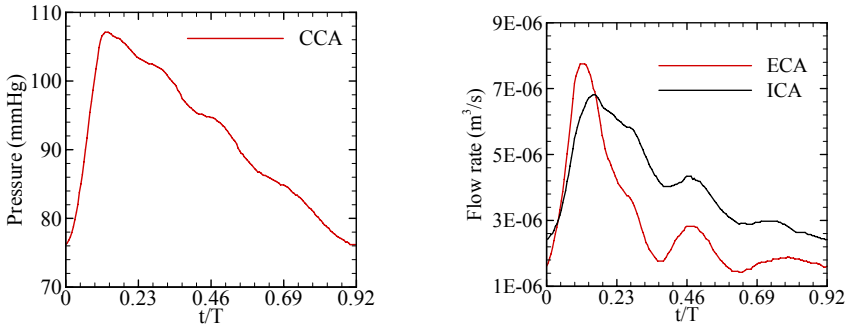

Fig. 7. Waveforms of assigned pressure and flow rates: (a) Pressure waveform at CCA; (b) Flow rate waveform at ICA and ECA.

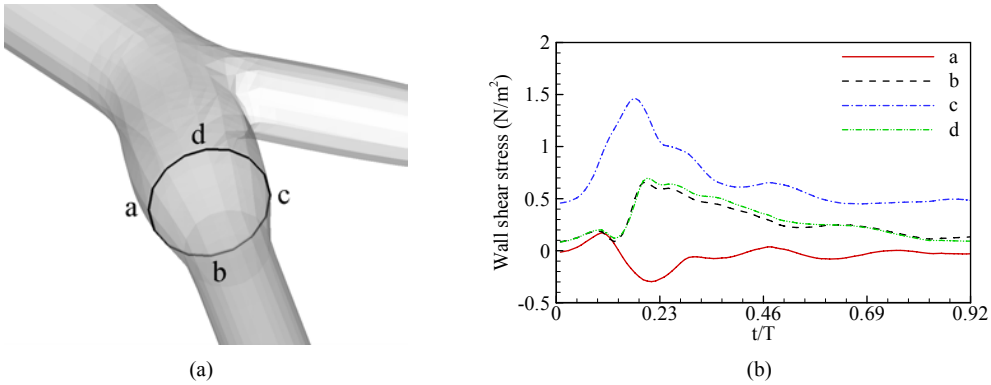

Fig. 8. Wall shear stress at section a: (a) Schematic of section a; (b) Temporal wall shear stress during the pulse cycle AT SECTION A.

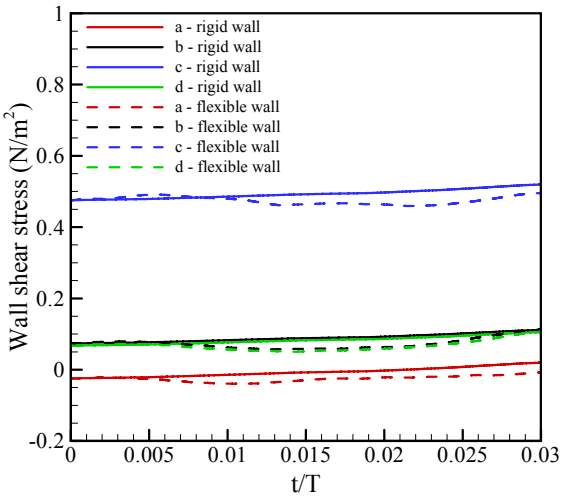

Fig. 9. Temporal wall shear stress.

Wall shear stress histories at several sites in the sinus are shown in Fig. 8. The wall shear stress profiles at the beginning of the cycle is similar to the assigned waveforms except for the outer wall of ICA. The temporal wall shear stress at outer wall of ICA indicates the existence of severe flow separation. Fig. 9 shows the temporal wall shear stress profile at the center of the sinus during the beginning of the cycle. The wall shear stresses of the flexible wall case are lower than those of the rigid wall case because the wall in the flexible wall case is distended.

4.3 Axial and secondary velocity field near the sinus

In the case of a flexible wall, a nearly incompressible isotropic wall property is considered. Thus, an elastic modulus of 3.0×10^5 Pa and Poisson's ratio of 0.49 are applied [9].

Instantaneous axial and secondary flow velocity fields at section A are shown in Fig. 10. The maximum axial velocity is skewed to the divider sinus wall due to the effect of the bifurcation angle, and reversed velocities are observed near the non-divider sinus wall. The bifurcation angle skews the axial velocity profile, a C-shaped axial velocity [25], to the divider sinus wall.

During accelerated flow, relatively small axial velocity difference is observed in flexible wall case. The magnitude of the secondary velocity is also smaller and the axial vortical motion is slightly different in the flexible wall case.

5. Conclusion

A numerical model for fluid-structure interaction was presented to simulate carotid bifurcation. The model was validated by comparison with wave propagation in a straight flexible tube. Numerical results showed fairly good agreement with previous calculations. The fluid velocity profiles in the

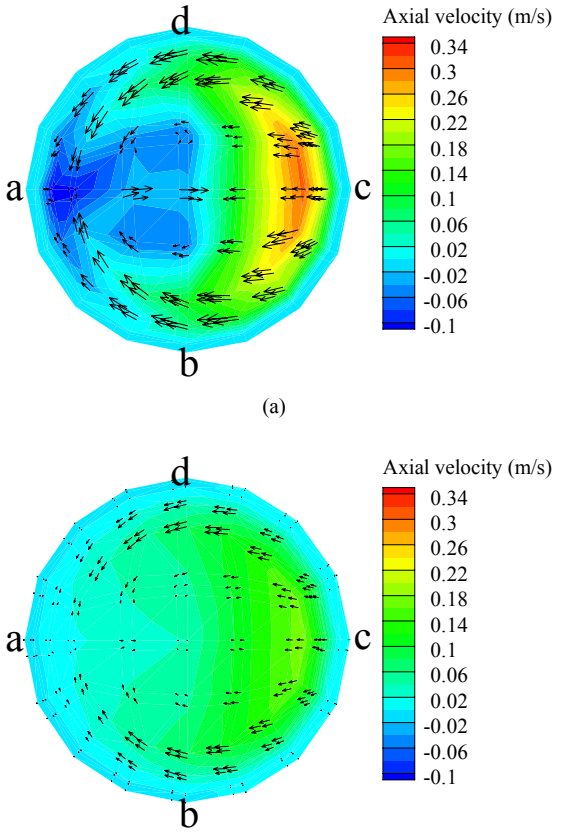

Fig. 10. Axial velocity profiles at section a t/t = 0.03: (a) rigid wall case; (b) flexible wall case.

carotid bifurcation sinus also showed good quantitative results when compared with previous numerical and experimental results. The skewed axial velocities for the geometrical shape at the sinus were shown. Wall shear stress at the outer wall of ICA has a remarkably low value, which means relatively high probability of atherosclerosis. In flexible wall case, the magnitudes of the axial and secondary velocity near the sinus are smaller than those of the rigid wall case during accelerated flow.

Acknowledgement

This work was supported by Mid-career Researcher Program and Priority Research Centers Program through the National Research Foundation of Korea (NRF) funded by the Ministry of Education, Science and Technology (2009-0079936 & 2010-0029613) and KISTI supercomputing center through the strategic support program for the supercomputing application research (KSC-2010-C1-0025).

Nomenclature

C : Convection matrix
D : Diameter of artery
D : Diffusion matrix
E : Young's modulus
F : Boundary integral term
G : Divergence matrix
K : Stiffness matrix
M : Mass matrix
n : Normal vector
p : Pressure
q : Weight function for continuity equation
Re : Reynolds number
u^s : Displacement vector of structure
v : Velocity vector
w : Weight function for momentum equations

Greek symbols

α_m, α_f, β, γ : Parameters of generalized-α method
ρ : Density
μ : Dynamic viscosity
ν : Poisson ratio
τ : Shear stress
ρ_∞ : Spectrum radius
σ : Stress

Superscript

f : Fluid region
s : Structure region
n : Time step

References

[1] C. G. Caro, J. M. Fitz-Gerald and R. C. Schroter, Atheroma and arterial wall shear observation, correlation and proposal of a shear dependent mass transfer mechanism for atherogenesis, *Proc. Roy. Soc. Lond. Biol.*, B 177 (1971) 109-159.
[2] B. K. Bharadvaj, R. F. Mabon and D. P. Giddens, Steady flow in a model of the human carotid bifurcation, Part I: Flow visualization, *J. Biomech.*, 32 (1982) 349-362.
[3] B. K. Bharadvaj, R. F. Mabon and D. P. Giddens, Steady flow in a model of the human carotid bifurcation, Part II: Laser-Doppler measurements, *J. Biomech.*, 32 (1982) 362-378.
[4] K. Perktold and M. Resch, Numerical flow studies in human carotid artery bifurcation: basic discussion of the geometric factor in atherogenesis, *J. Biomed. Eng.*, 12 (1990)111-123.
[5] K. Perktold, R. O. Peter, M. Resch and G. Langs, Pulsatile non-Newtonian flow in three-dimensional carotid bifurcation models: a numerical study of flow phenomena under different bifurcation angles, *J. Biomed. Eng.*, 13 (1991) 507-515.
[6] K. Perktold and G. Rappitsch, Computer simulation of local blood flow and vessel mechanics in a compliant carotid artery bifurcation model, *J. Biomech.*, 28 (1995) 845-856.
[7] D. N. Ku and D. P. Giddens, Pulsatile flow in a model carotid bifurcation, *Arteriosclerosis*, 3 (1983) 31-39.
[8] S. A. Urquiza, P. J. Blanco, M. J. Venere and R. A. Feijoo,

Multidimensional modelling for the carotid artery blood flow, *Comput. Meth. Appl. Mech. Engrg*., 195 (2006) 4002-4017.

[9] C. S. Kim, C. Kiris, D. Kwak and T. David, Numerical simulation of local blood flow in the carotid and cerebral arteries under altered gravity, *J. Biomech. Eng*., 128 (2006) 194-202.

[10] K. W. Lee and X. Y. Xu, Modelling of flow and wall behaviour in a mildly stenosed tube, *Med. Eng. Phys.,* 24 (2002) 575-586.

[11] W. K. Liu, Y. Liu, D. Farrell, L. Zhang, X. S. Wang, Y. Fukui, N. Patankar, Y. Zhang, C. Bajaj, J. Lee, J. Hong, X. Chen and H. Hsu, Immersed finite element method and its applications to biological systems, *Comput. Meth. Appl. Mech. Engrg.*, 195 (2006) 1722-1749.

[12] G. Guidoboni, R. Glowinski, N. Cavallini and S. Canic, Stable loosely-coupled-type algorithm for fluid-structure interaction in blood flow, *J. Comp. Phys.,* 228 (2009) 6916-6937.

[13] E. Kuhl, S. Hulshoff and R. de Borst, An arbitrary Lagrangian Eulerian finite element approach for fluid-structure interaction phenomena, *Int. J. Numer. Meth. Engrg*., 57 (2003) 117-142.

[14] H. G. Kim, A new coupling strategy for fluid-solid interaction problems by using the interface element method, *Int. J. Numer. Meth. Engrg*., 81 (2010) 403-428.

[15] R. Codina, E. Oňate and M. Cervera, The intrinsic time for the streamline upwind/Petrov-Galerkin formulation using quadratic elements, *Comput. Meth. Appl. Mech. Engrg*., 94 (1992) 239-262.

[16] J. Chung and G. M. Hulbert, A time integration algorithm for structural dynamics with improved numerical dissipation: the generalized-α method, *J. Appl. Mech*., 60 (1993) 371-375.

[17] K. E. Jansen, C. H. Whiting and G. M. Hulbert, A generalized-α method for integrating the filtered Navier-Stokes equations with a stabilized finite element method, *Comput. Meth. Appl. Mech. Engrg*., 190 (2000) 305-319.

[18] C. J. Greenshields and H. G. Weller, A unified formulation for continuum mechanics applied to fluid-structure interaction in flexible tubes, *Int. J. Numer. Meth. Engrg*., 64 (2005) 1575-1593.

[19] Y. Bazilevs, V. M. Calo, Y. Zhang and T. J. R. Hughes, Isogeometric fluid-structure interaction analysis with applications to arterial blood flow, *Comput. Mech*., 38 (2006) 310-322.

[20] C. S. Jog and R. K. Pal, A monolithic strategy for fluid-structure interaction problems, *Int. J. Numer. Meth. Energ.,* 85 (2011) 429-460.

[21] S. Kang, H. G. Choi and J. Y. Yoo, Investigation of unsteady fluid-structure interactions using a velocity-linked P2/P1 finite element method and generalized-α method, *Int. J. Numer. Meth. Eng.* (accepted for publication).

[22] F. J. H. Gijsen, F. N. van de Vosse and J. D. Janssen, The influence of the non-Newtonian properties of blood on the flow in large arteries: steady flow in a carotid bifurcation model, *J. Biomech*., 32 (1999) 601-608.

[23] S. Tada and J. M. Tarbell, A computational study of flow in a compliant carotid bifurcation—stress phase angle correlation with shear stress, *Ann. Biomed. Engrg.,* 33 (2005) 1219-1229.

[24] K. Perktold, M. Resch and R. O. Peter, Three-dimensional numerical analysis of pulsatile flow and wall shear stress in the carotid artery bifurcation, *J. Biomech.,* 24 (1991) 409-420.

[25] C. C. M. Rindt, A. A. van Steenhoven, J. D. Janssen, R. S. Reneman and A. Segal, A numerical analysis of steady flow in a three-dimensional model of the carotid artery bifurcation, *J. Biomech.,* 23 (1990) 461-473.

Hyoung-gwon Choi received a Ph.D at Seoul National University, Korea, in computational fluid dynamics based on finite element method. He is currently an associate professor of the Department of Mechanical and Automotive Engineering of Seoul National University of Science and Technology, Korea.